Boundary-layer analysis of waves propagating in an excitable medium: Medium conditions for wave-front–obstacle separation

J. M. Starobin* and C. F. Starmer
Departments of Medicine (Cardiology) and Computer Science, Duke University Medical Center, Durham, North Carolina 27710
(Received 11 September 1995; revised manuscript received 4 March 1996)

In an excitable medium, wave breaks are essential for spiral wave formation. Although wave breaks can result from collisions between a wave and an obstacle, it is only when the resultant wave fragments separate from the obstacle (wave-front–obstacle separation) that a spiral wave will begin to develop. We explored collisions between a piecewise linear obstacle and an incident wave front while varying the excitability of the media and the angle between the linear obstacle segments. Wave-front–obstacle separation was observed to occur within the small boundary layer of the order of the wave-front thickness. Conditions for wave-front–obstacle separation were determined by the relationship between reaction-diffusion flows within this boundary-layer region. We developed a theoretical characterization of the boundary-layer region that permits estimation of the critical values of medium parameters and obstacle geometry that define the transition from wave-front–obstacle attachment to wave-front–obstacle separation. Theoretical predictions revealed good agreement with results of the numerical simulations. [S1063-651X(96)00707-6]

PACS number(s): 47.32.Cc, 87.22.−q, 82.40.Ck, 87.10.+e

Wave propagation in many chemical and biological media can be described in terms of a nonlinear reaction-diffusion equation [1]. Waves are created by a stimulus that switches a small portion of the medium from a ''rest'' state to an ''excited state.'' If the stimulus is below a certain threshold, either no wave is created or the wave collapses. If the stimulus is larger than this threshold, a wave propagates away from the stimulus site and then dies at the boundary of the medium. However, if the wave is fragmented (broken), perhaps secondary to a collision with an unexcitable obstacle, there are two possible outcomes: either the wave fragments maintain contact with the obstacle boundary [Fig. 1(A)] or the fragments separate from the obstacle boundary [Fig. 1(B)] forming a spiral wave similar to that observed in chemical media [2] and in cardiac tissue [3]. Although the evolution of wave breaks following wave-front–obstacle collisions has been studied numerically [4–8] and experimentally [9,10], the conditions that determine the subsequent fate of a wave fragment remains unclear.

For many excitable media including cardiac tissue, the diffusion fluxes coupling neighboring elements of excitable media reside within the wave front of thickness L_f which is much smaller than the length of the excitation wave. The dynamics of such waves can be described by the kinematic theory when the wave-front radius of curvature is larger than both the wave-front thickness and the distance between the wave front and wave back [11]. For a broken wave, the local radius of curvature at each tip is comparable to the wave-front thickness and much smaller than the length of the wave itself. Consequently analysis of the tip movement of a recently fractured wave is beyond the assumptions of the kinematic theory.

Seeking a more comprehensive understanding of a mechanism of wave tip motion following the wave-front–obstacle collisions, we focused on developing a different approach which permitted us to describe the behavior of the boundary layer between a piecewise linear obstacle and a colliding excitation wave. The main idea behind our approach was to partition this boundary layer into small regions and analyze the fluxes that flowed between the wave-front regions and the adjacent ''rested'' regions. Using this strategy, we found that the transition between wave-front–obstacle separation and wave-front–obstacle attachment depended on a critical balance of the reaction-diffusion flows within a boundary layer of the order of the wave-front thickness.

Numerical studies of wave-front–obstacle interactions demonstrated that the possibility of wave-front–obstacle separation occurred during the initial moments of front formation at the obstacle boundary and was influenced by the medium ''excitability,'' i.e., the magnitude of a perturbation required to initiate a propagating wave [6].

Here we consider the nonlinear reaction-diffusion equations of the FitzHugh-Nagumo class

$$\frac{\partial u}{\partial t} = \frac{\partial^2 u}{\partial x^2} + \frac{\partial^2 u}{\partial y^2} + f(u) - V, \tag{1}$$

$$\frac{\partial V}{\partial t} = \varepsilon(\gamma u - V), \tag{2}$$

where $u(x,y,t)$ is a dimensionless function similar to the transmembrane potential in a biological excitable cell and $V(x,y,t)$ is a dimensionless function similar to a slower recovery current. Using this electrical analogy, we consider reaction-diffusion fluxes to be the flow of a charge (current) down a potential gradient. Excitability is determined by the nonlinear function $f(u)$ that represents the reactive properties of the medium and to some extent by ε, the ratio of fast to slow time constants. We consider $f(u)$ as a piecewise linear function similar to the current-voltage relationship of a nonlinear oscillator [Fig. 2(A)]. The slope of this function λ

*Author to whom correspondence should be addressed. Fax: (919)684-8666. Electronic address: josef@hodgkin.mc.duke.edu

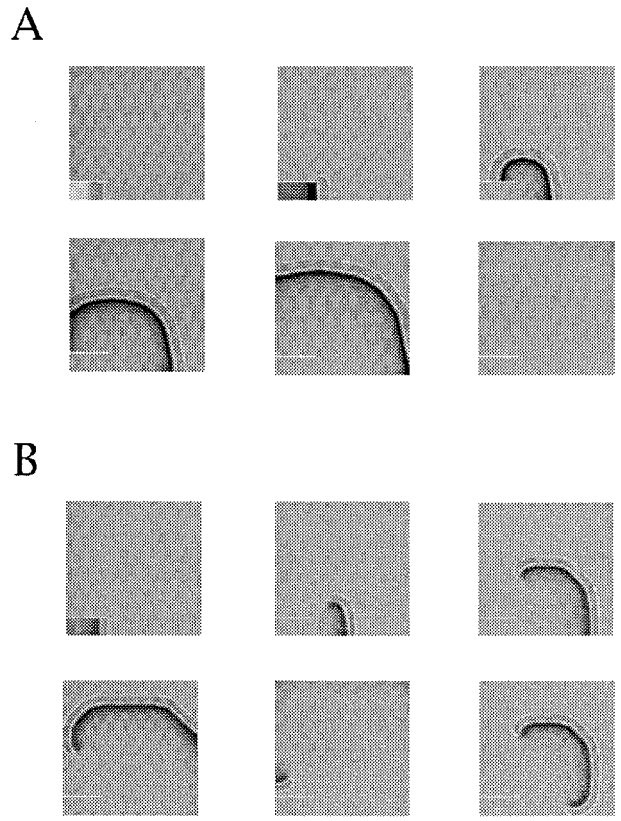

FIG. 1. Panels A and B show the computed temporal evolution of an excitation wave (left to right, top to bottom) for different excitabilities λ following the collision with an unexcitable obstacle. We solved the reaction-diffusion system [Eqs. (1), (2)] numerically with no-flux boundary conditions at the medium boundary and obstacle surface. We used the implicit locally one-dimensional fractional step difference scheme [14] with a second order approximation on the space grid interval Δx and a first-order approximation on the time grid interval Δt. We used $\Delta t=0.2$ and $\Delta x=\Delta y=0.25$ for a 300×300. The medium parameters were $\varepsilon=0.01$, $\gamma=7$, $m_1=0$, $m_2=0.85$, $m_3=3.2$, $\alpha=2.76$. For these parameters, the critical value of λ at the transition from wave-front–obstacle attachment to wave-front–obstacle separation was $\lambda_{crit}=0.86$. In panel A, $\lambda=0.91>\lambda_{crit}$, and this sequence shows that as the wave passes the obstacle, wave-front–obstacle attachment is maintained and eventually the wave propagates toward the medium boundaries and dies. In panel B, $\lambda=0.77<\lambda_{crit}$ and it is seen that as the wave front passes the end of the obstacle, there is an insufficient charge within the wave front to maintain wave-front–obstacle attachment. Consequently, as the wave passes beyond the obstacle, the wave front and the obstacle separate (the wave tip is ''pulled'' from the obstacle) with subsequent formation of a spiral wave.

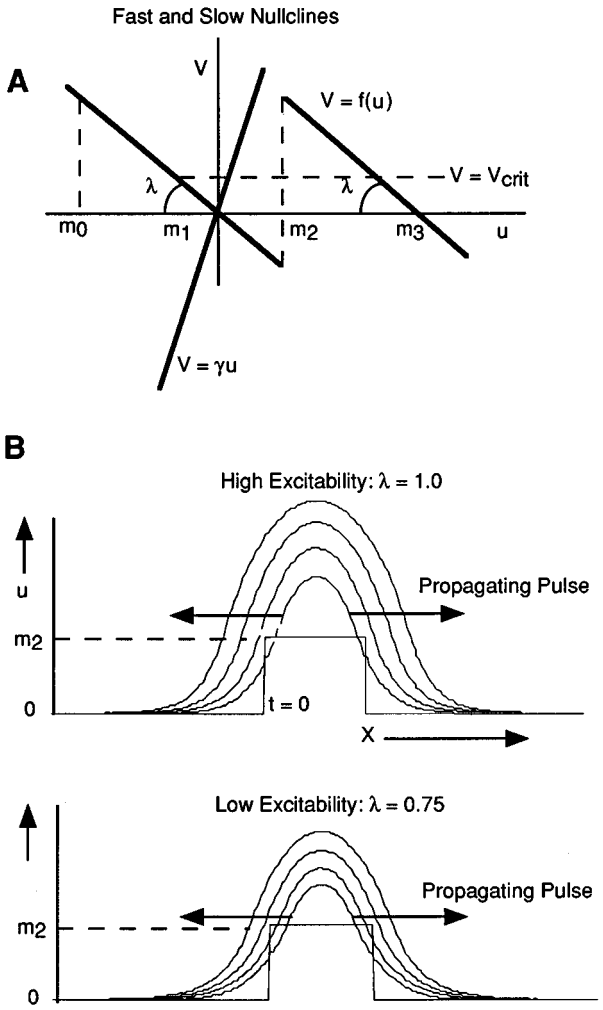

FIG. 2. Panel A illustrates the null clines of the reaction-diffusion system. We consider u as similar to the transmembrane potential of an excitable cardiac or nerve cell, $f(u)$ is similar to the current-voltage relationship of the cellular excitation process and V is similar to the slow recovery current. The function $f(u)$ is a piecewise linear function, where the slope of each linear element λ refers to the rate of the fast excitation process and influences media excitability. The slope γ refers to the rate of the slow recovery process. Panel B illustrates the relationship between the medium excitability, as determined by λ, and the excitation wave. The potential $u(x)$ is shown for the initial condition ($t=0$, rectangular pulse) and at four later times. An initial condition of $v(x,t=0)=m_2$ for a short stimulation region. At subsequent times, the potential can be seen to increase in amplitude (to m_3) as well as propagating away from the stimulation site. For high excitability $\lambda=1.0$ the wave develops more rapidly and propagation velocity is greater than for the smaller value $\lambda=0.75$.

controls one aspect of excitability by determining the maximum current that is available to excite adjoining regions of the medium: larger values of λ result in a more excitable medium while smaller values of λ result in a less excitable medium [Fig. 2(B)]. Excitability is also influenced by m_1, m_2, and m_3, the zeros of $f(u)$ with respect to the equilibrium value of the recovery variable V_{eq}. A highly excitable medium is determined by $m_2-m_1 \ll m_3-m_1$. The factors γ and ε, are relaxation parameters and $\varepsilon \ll 1$.

We consider several additional properties of an excitable medium that are essential for our analysis: the critical region L_D which is the minimum region of the medium that must be excited before a wave front can avoid collapsing [Fig. 3(A)]; and the critical value of V, V_{crit} associated with wave-front propagation with a velocity of zero [Fig. 3(B)]. The critical excitation region L_D is related to the minimal wave-front thickness of a stationary propagating wave, where L_{crit} is the wave-front thickness associated with the

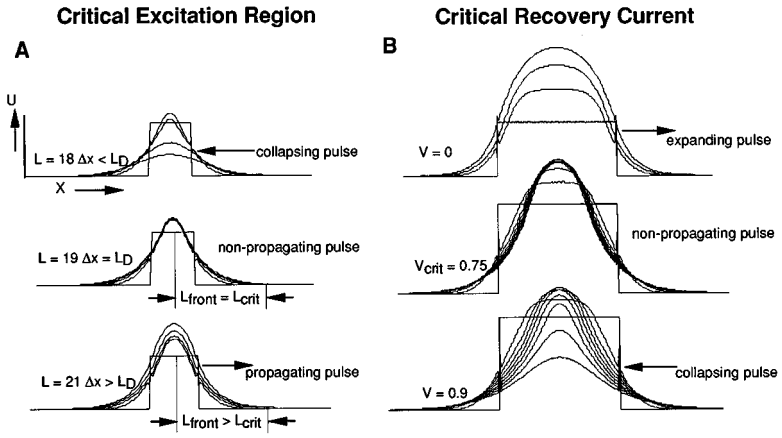

FIG. 3. Panels A and B demonstrate the relationship between the critical values of the recovery current V_{crit} minimal excitation length L_D for propagation of an excitation pulse and the front thickness L_f. Panel A illustrates the sensitivity of successful propagation with respect to the size $(n\Delta x)$ of the excited region. The rectangular pulse represents the initial condition. When the length of the excited region $L<L_D$ the excitation pulse collapses (top of panel A, $L<L_D$) and when the length of the excited region $L>L_D$ the excitation pulse grows and propagates away from the stimulation site (bottom of panel A). Excitation of the critical length L_D (panel A, middle) results in formation of a nonpropagating excitation pulse of minimal thickness $2L_{\text{crit}}$. Panel B illustrates the effect of the recovery current on propagation of a trigger wave ($\varepsilon=0$). For $V<V_{\text{crit}}$, excitation results in an expanding wave away from the stimulation region (top curves). When $V>V_{\text{crit}}$ the initial excitation results in a collapsing wave (bottom). When $V=V_{\text{crit}}$ the resulting pulse does not propagate and this condition reflects a perfect balance between the reaction and diffusion charges feeding the front region and the loss of charge into the adjacent rested medium. In this case, the wave front thickness is equal to $2L_{\text{crit}}$ as shown in panel A (different scale).

zero propagation velocity [12]. The critical value of the recovery current V_{crit} occurs when the area of $f(u)$ between m_1 and m_2 is equal to the area of $f(u)$ between m_2 and m_3 [11].

Figure 4 illustrates the temporal evolution (panels 1–6) of a wave-front–obstacle collision leading to a wave-front–obstacle separation as the wave passes the end of the obstacle. Panels 1–3 reveal curling of the wave front around the corner of the obstacle and extension of the wave-front tip adjoining the obstacle surface. Tip extension temporarily halts at the corner of the obstacle (panels 3 and 4) while the rest of the wave front continues to propagate. During the time that the wave tip is developing near the corner, the wave back approaches the tip region (panels 4,5). Only after the wave back reaches the end of the obstacle does the entire wave pull away from the obstacle corner (panel 6).

Focusing on tip formation and the movement seen in panels 3–5 (Fig. 4), we see that the incident wave separates from the obstacle when the portion of the wave-front tip adjacent to the corner of the obstacle has zero velocity oriented parallel to the obstacle boundary. Under conditions of zero velocity, the wave-front thickness is not that of a stationary propagating wave L_f but is equal to the smaller critical value of the wave-front thickness L_{crit} described above. The wave front at the obstacle corner shown in panels 3 and 4 forms a thin (relative to the length Λ of the whole wave) boundary layer with thickness on the order of L_{crit} which separates the excited and unexcited portion of the medium near the obstacle corner.

In order to simplify the analysis of the diffusion fluxes within the boundary layer we discretized it with squares of order L_{crit} which formed a piecewise rectangular approximation of the boundary layer with a characteristic curvature $<1/L_{\text{crit}}$ (Figs. 5, 6). We assumed that the spatial potential gradient $(m_3-m_1)/L_{\text{crit}}$ was constant within the boundary layer during its formation time T while the boundary-layer area A_L and perimeter P_L increased as a step function of time as shown in Figs. 5(D), 6(C). The accuracy of this approximation is of the order of $\varepsilon^2\sim(L_{\text{crit}})^2/(\Lambda)^2$ in space and ε in time.

Whether the wave front ''sticks'' to or separates from the obstacle boundary depends on what we call a charge balance derived from the integral form of Eqs. (1), (2) obtained by averaging them in time over T

$$C_B=Q_S-Q_L, \tag{3}$$

where Q_S represents both the ''source'' charge available within the incident wave front of length L_f and the charge developed by the reaction within the boundary layer of length L_{crit} and Q_L represents the ''load'' charge requirements that must be overcome in order to ignite the boundary layer. The diffusive charge that flows from the wave-front region A_S is determined by the time average potential gradient between the wave front $[u=(m_1+m_3)/2]$ and the boundary layer $(u=m_1)$ so that

$$Q_{SD}=A_S(m_3-m_1)/2, \tag{4}$$

where $A_S\sim L_f^2$ is the area of the incident wave front adjacent to the obstacle surface. Due to the near zero velocity of the boundary layer, recovery current $\Delta V=(V-V_{eq})$ develops within the boundary-layer region of area A_L with the same time scale as the excitation process [13]. Assuming ΔV to be equal to $(V_{\text{crit}}-V_{eq})$ and constant over T, this amount of charge must be offset by the reaction part of the source charge described by

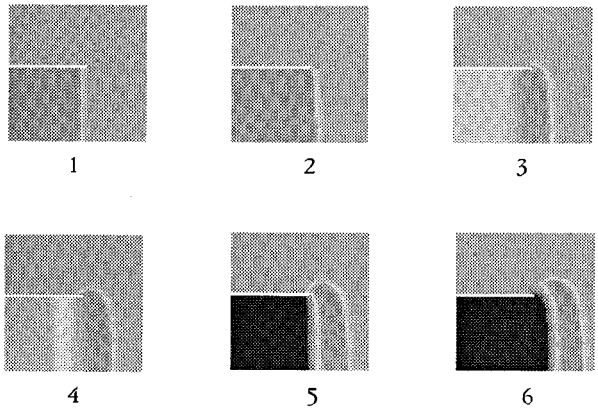

FIG. 4. The temporal sequence of wave-front–obstacle interaction resulting in separation of the excitation wave from the obstacle (time sequence corresponds to panel numbers 1–6). Panels 1–3 show the initial curling of the wave front around the corner of the obstacle and development of the wave tip (load boundary layer) adjoining the obstacle surface. In panels 2–4, the tip remains relatively stationary at the end of the obstacle while the rest of the wave continues to propagate, thus extending the tip in the direction of the incident wave. As the wave back passes the end of the obstacle corner (panel 5) the tip can be seen to be fully formed. As the wave continues to propagate, the tip eventually is unable to maintain contact with the obstacle boundary and becomes unattached (panel 6). The slower propagation of the tip results in curling and formation of a spiral similar to that displayed in Fig. 1(B). In order to demonstrate separation for a different set of parameters (compared to those used in Fig. 1), for this illustration we used $\lambda=0.98$, $\varepsilon=0.03$, $\alpha=2.76$, where $\lambda_{\text{crit}}=1.13$.

$$Q_{SR}=A_L(V_{\text{crit}}-V_{eq}), \tag{5}$$

where $A_L \sim L_{\text{crit}}^2$ the time average area of the developing load boundary layer.

The load charge requirement is defined as the charge that leaks from the perimeter of the boundary layer,

$$Q_{LL}=P_L(m_3-m_1)/L_{\text{crit}}, \tag{6}$$

where $P_L \sim L_{\text{crit}}$ is the time average perimeter of the load boundary layer exposed to the adjacent medium at equilibrium conditions. With these components we can write the equation for C_B as

$$C_B=Q_{SD}+QSR-Q_{LL},$$

$$C_B=A_S(m_3-m_1)/2+A_L(V_{\text{crit}}-V_{eq})-P_L(m_3-m_1)/L_{\text{crit}}. \tag{7}$$

In order to remove the dependencies of A_S, A_L, and P_L on the wave-front lengths L_f and L_{crit} we divide and multiply each coefficient by its respective measure. After substituting the values of L_f^2, L_{crit}^2 and L_{crit} from Appendix A into (7), we get

$$C_B=\chi^{-1}\left\{\left[\frac{A_L}{L_{\text{crit}}^2}-\frac{P_L}{2\sigma^2 L_{\text{crit}}}\frac{\alpha+1}{\alpha-1}\right]\lambda^3+\frac{A_s}{L_f^2}\frac{(\alpha+1)^3}{4\alpha(\alpha-1)}\lambda^2 -\varepsilon\frac{A_s\gamma(\alpha+1)^5\sigma}{L_f^2 4\alpha^2(\alpha-1)}\right\},$$

$$\chi=\frac{(\alpha+1)\lambda^3}{2(m_3-m_1)\sigma^2(\alpha-1)}, \tag{8}$$

which describes the balance between the source charge and the charge required to excite the boundary-layer region. The area and perimeter functions are determined by the angle of the obstacle θ relative to the wave front as described in Appendix B.

Formula (8) indicates that the transition between wave-front–obstacle separation and wave-front–obstacle attachment, i.e., where $C_B=0$, can be altered by varying any of the medium parameters. When $C_B>0$, there is sufficient diffusion charge within the wave front and reaction charge within the boundary layer to overcome the charge that leaks from the boundary layer resulting in extension of the wave tip. When $C_B<0$, there is insufficient wave-front charge to overcome the demands for wave tip extension, resulting in wave-front–obstacle separation. In terms of the wave velocity, when $C>C_{\text{crit}}(C_{\text{crit}}=C|_{\lambda=\lambda_{\text{crit}}})$ then $C_B>0$, and propagation around the corner at the wave-front–obstacle boundary succeeds while when $C<C_{\text{crit}}$, then $C_B<0$ and local propagation at the corner of the obstacle–wave-front interface fails and the wave separates from the obstacle.

For a range of medium parameters $(\varepsilon,\gamma,\alpha,\lambda,\theta)$ we can use $C_B=0$ to determine critical contours (e.g., as a function of ε and λ) that separate regions of wave-front–obstacle attachment from regions of wave-front–obstacle separation, i.e., where C_B is equal to zero.

We evaluated the accuracy of the critical propagation velocity, C_{crit} derived from the roots of $C_B=0$, by comparison with the numerical estimates of C_{crit} associated with the transition from wave-front–obstacle attachment to wave-front–obstacle separation. Figures 7(A), 7(B) illustrates the theoretical predictions [we evaluated Eq. (8) with $C_B=0$, to compute λ_{crit} and Eq. (A2) to compute C_{crit}] and the numerically determined values (circles, squares) for different angles θ. These experiments revealed good agreement for values of $\varepsilon<0.04$.

Our choice of a piecewise linear obstacle was motivated by the desire to understand the general role of the obstacle curvature in altering the wave tip charge balance between the source Q_S and the load Q_L. In addition to simple piecewise linear obstacles, theoretical predictions allow us to estimate the critical separation parameters for obstacles of an arbitrary shape. Since we found that separation evolves within the boundary layer which is of the order L_f, the obstacle boundary can be approximated by small linear segments of the order of L_f. The local angle θ between linear segments can be readily linked to a local curvature radius R_{curv} associated with the local angle apex

$$R_{\text{curv}}=\frac{L_f}{2\sin(\theta/2)}. \tag{9}$$

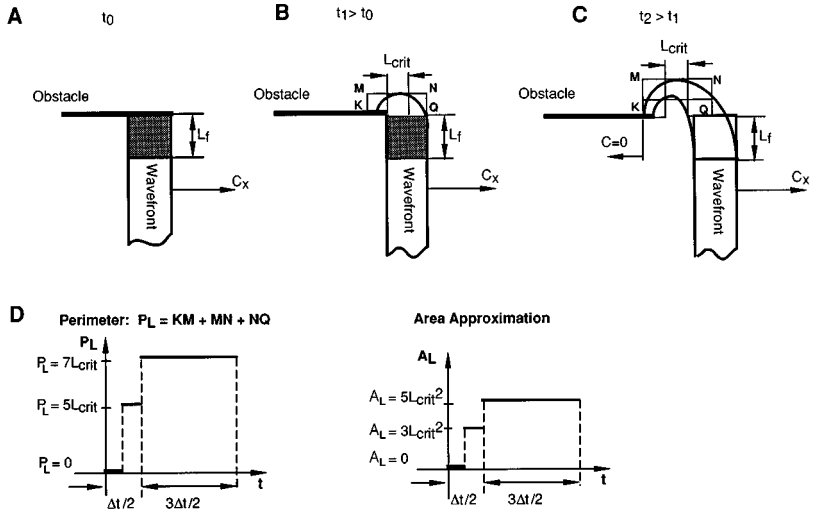

FIG. 5. Schematic representation of the relationship between the source region within the wave front and the temporal formation of the boundary layer following the collision between a wave and an obstacle oriented parallel to the wave velocity ($\theta=\pi$). Panels A and B show source regions (squares of area $A_S=2L_f^2$ with shading) formed by a portion of the incident wave front (wave-front thickness L_f) adjacent to the obstacle surface. Panel B $t=t_1$ shows the intermediate location of the wave front as it advances around the obstacle corner. During this time charge flows out from the source region and forms the first portion of the boundary layer with an area $3(L_{\rm crit})^2$ equal to that for $\theta=\pi/2$. While time increases to $t=t_2$ (panel C) the boundary layer continues to grow forming a tip sticking near the obstacle corner. The whole boundary-layer region is approximated by a piecewise (5 squares) rectangular strip with a width equal to $L_{\rm crit}$ and an area equal to $5(L_{\rm crit})^2$. The leading edge of the boundary layer is formed by linear segments KM, MN, and NQ. The propagation velocity of the KM segment is equal to zero. The perimeter of the leading edge of the boundary layer P_L and its area A_L extend as step functions of t changing in time as shown in panel D during the boundary layer formation time $t_2-t_0=2\Delta t$.

This equation highlights the relationship between the wave-front properties and the curvature of the obstacle. When the local radius of curvature of the obstacle is smaller than that defined by Eq. (9), then following a wave-front–obstacle collision, wave-front–obstacle separation will occur and a spiral wave will possibly develop.

Pertsov and co-workers [6,7] were the first to note with numerical studies, the critical role excitability played in events following wave-front–obstacle collision and that events occurring within the wave front at the wave tip were potentially important. Following these initial observations, Agladze *et al.* [9] experimentally probed the nature of wave–obstacle collisions using the Belousov-Zhabotinsky (BZ) reagent in a medium containing obstacles. They demonstrated that for a fixed angle of incidence between the wave front and obstacle, there was a critical excitation frequency (> control frequency) where the wave-front–obstacle separation occurred and new spirals formed. Our interpretation is that the increased frequency of excitation resulted in a slowed propagation and an obligatory reduction

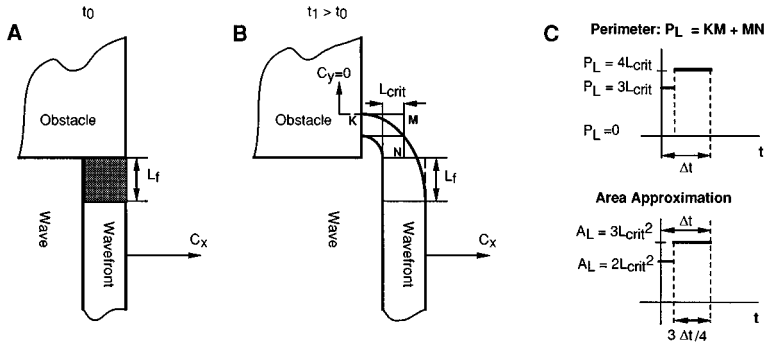

FIG. 6. Formation of a load boundary layer for the piecewise unexcitable obstacle with a right angle $\theta=\pi/2$ between its linear segments. Panel A $t=0$ shows a source region (square of area $A_S=L_f^2$ with shading) formed by a portion of the incident wave front (wave-front thickness L_f) adjacent to the obstacle surface. Panel B $t=\Delta t$ shows the wave front advanced behind the obstacle corner. During this time the charge flows out from the source region and forms the load boundary layer between the obstacle surface and the incident wave front. The fully developed boundary layer region is approximated by a piecewise (3 squares) rectangular strip with a width equal to $L_{\rm crit}$ and area equal to $3L_{\rm crit}{}^2$. The leading edge of the boundary-layer region is formed by the linear segments KM and MN. A propagation velocity of the KM segment is equal to zero. The perimeter of the leading edge of the boundary layer P_L and its area A_L extend as step functions of t changing in time as shown in panel C during the boundary layer formation time $t_1-t_0=\Delta t$.

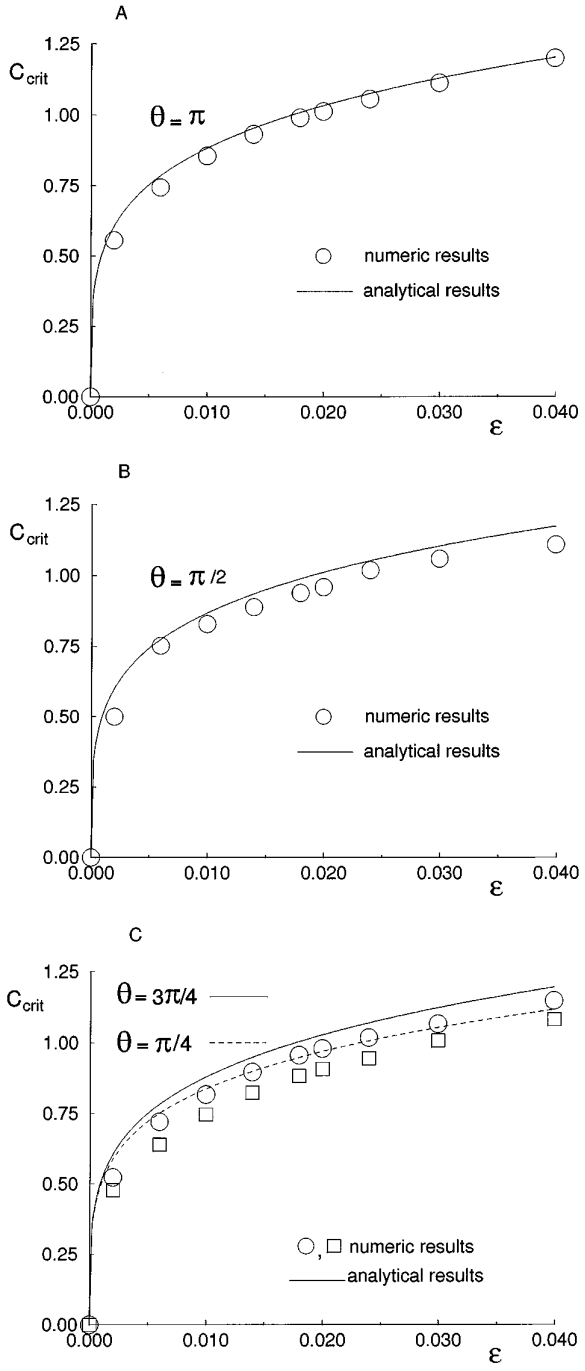

FIG. 7. The dependence of the critical wave-front propagation velocity C_{crit} for wave-front–obstacle separation, as a function of the model parameter ε while $\gamma=7$ and $\alpha=2.76$. Solid and dashed lines represent the analytical approximation of C_{crit} where λ_{crit} is the root of $C_B=0$, and the circles and squares represent numerically determined values. Each curve of C_{crit} as a function of ε separates the plane into two regions: (1) for wave-front velocities below the line, a wave-front–obstacle separation occurs; and (2) for wave-front velocities above the line, a wave-front–obstacle attachment is maintained. Panel A illustrates this dependence for an obstacle aligned parallel to the incident wave velocity vector ($\theta=\pi$). Panel B illustrates this dependence for an obstacle aligned perpendicular to the incident wave velocity vector ($\theta=\pi/2$). Panel C illustrates the interpolated dependence for obstacles with intermediate angles $\theta=\pi/4$ and $\theta=3\pi/4$. The numerical experiments reveal good agreement with the analytical approximation for all angles.

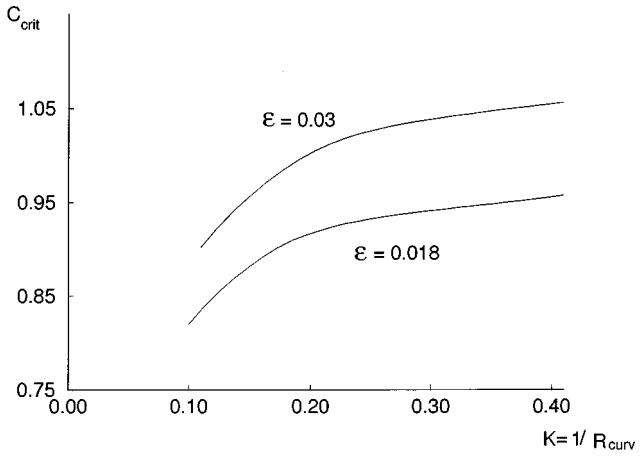

FIG. 8. The dependence of the critical velocity C_{crit} associated with the wave-front–obstacle separation on the local obstacle curvature $K=1/R_{\mathrm{curv}}$ for different ε. Here R_{curv} is the local curvature radius which is given by (9) and $\gamma=7$, $\alpha=2.76$ are the medium parameters.

in L_f until the critical value (associated with separation) was achieved. Similarly, in studies of the interaction of a wave in the BZ medium with a fixed obstacle of varying curvature, Gomez-Gesteria *et al.* [10] showed that varying the excitability altered the critical angle at which wave-front–obstacle separation occurred. The dependence of C_{crit} on $K=1/R_{\mathrm{curv}}$ shown in Fig. 8 is in qualitative agreement with the experimental observations in the BZ excitable medium[10].

In conclusion, the present analysis indicates that wave-front–obstacle separation occurs within the small boundary layer that links the wave tip with the obstacle surface. Conditions for wave-front–obstacle separation are determined by the relationship between the reaction-diffusion flows within the boundary-layer region which is of the order of the wave-front thickness. The transition between wave-front–obstacle separation and wave-front–obstacle attachment can be altered by varying any of the medium parameters or the obstacle geometry. The present theoretical study permits a comprehensive determination of the critical values of the medium parameters and obstacle geometry for wave-front–obstacle separation, which was an open problem.

ACKNOWLEDGMENTS

We wish to acknowledge the critical assistance provided by V. I. Krinsky, V. N. Biktashev, and A. M. Pertsov. Their critical reviews and discussions were helpful in clarifying our results. This research was supported in part by Grant No. HL32994 of The National Heart, Lung and Blood Institute, NIH.

APPENDIX A

In [12], we derived one-dimensional (1D) estimates for the wave-front thickness L_f, the front thickness of a wave propagating at zero velocity L_{crit}, and the critical value of the recovery variable associated with zero velocity [for a piecewise linear f(u) shown in Fig. 2], V_{crit} which are given by

$$L_f=\sigma\left(\frac{C^2+4\lambda}{\lambda}\right)^{1/2},$$

$$L_{\rm crit}=2\sigma/\sqrt{\lambda},$$

$$V_{\rm crit}-V_{eq}=\lambda(m_2-m_1)\,\frac{\alpha-1}{2},$$

$$\alpha=\frac{m_3-m_2}{m_2-m_1},$$

$$\sigma=\ln[M^{-1}(m_3-m_1)], \tag{A1}$$

where C is the pulse velocity in a 1D excitable cable [for $f(u)$ shown in Fig. 2] and m_1, m_2 and m_3 are the zeros of $f(u)$ with respect to V_{eq}. For the 2D boundary layer analysis used here, we assume the 1D front parameters to be equal to the 2D boundary layer parameters.

The factor σ is a constant which defines the end points of the exponential wave front which are required to estimate L_f and $L_{\rm crit}$ [12]. The factor M is a threshold that defines where the wave-front starts (m_1+M) and ends (m_3-M), respectively. The value of the threshold relates to a certain K-fold change in the wave-front amplitude m_3-m_1. Here we used the value $\sigma=1+\ln 2$ which is associated with an e-fold change.

Under the conditions when the wave-front thickness of the incident wave is sufficiently large (high excitability) one can estimate the incident wave velocity from that of a trigger wave, a wave that propagates while the slow recovery current remains at the equilibrium value $V_{eq}(\varepsilon=0)$. For the piecewise linear $f(u)$ shown in Fig. 2 this velocity C_0 is given by[12]

$$C_0=(\alpha-1)\sqrt{\lambda/\alpha}. \tag{A2}$$

When the medium properties are near the separation–no separation boundary, it is necessary to adjust for the influence of the slow recovery current V on wave-front velocity. It was shown in [12] that the recovery current increases during the front formation time $\tau=L_f(C_0)/C_0$ by an amount: $\Delta V=\varepsilon\gamma(m_3-m_1)\tau$. Using (A1) and (A2) and rewriting ΔV in terms of medium parameters we get

$$\Delta V=\varepsilon\gamma\sigma(m_3-m_1)\,\frac{\alpha+1}{\lambda(\alpha-1)}. \tag{A3}$$

From this equation, we estimate new roots m_i^* of $f(u)$ with respect to $V_{eq}+\Delta V$ which provides a value of excitability α^*.

$$\begin{aligned}\alpha^*&=(m_3-m_2-\Delta V/\lambda)/(m_2-m_1+\Delta V/\lambda)\\&=\{\alpha-\Delta V/[\lambda(m_2-m_1)]\}/\{1+\Delta V/[\lambda(m_2-m_1)]\}.\end{aligned} \tag{A4}$$

Expanding $\{1+\Delta V/[\lambda(m_2-m_1)]\}^{-1}$ and keeping only the first-order term, the adjusted velocity can be written using Eq. (A2) as

$$C=C_0-\zeta\varepsilon \quad \text{where} \quad \zeta=\sigma\,\frac{\gamma(\alpha\lambda)^{-3/2}}{2}\,\frac{(\alpha+1)^4}{\alpha-1}. \tag{A5}$$

APPENDIX B

We will seek functions A_S, P_L and A_L in terms of a biquadratic polynomial on $\langle S\rangle=S(\theta)/L_f^2$, $\phi_i(\theta)=F_i+G_i\langle S\rangle^2+H_i\langle S\rangle^4$, where $S(\theta)$ is the area of the source region as a function of θ. Coefficients F_i, G_i and H_i are unknown constants ($i=1,2,3$ for A_S, P_L and A_L, respectively) which can be determined, for instance, from the charge balance for three particular angles: $\theta=0$, $\theta=\pi$, and $\theta=\pi/2$.

We assume that for intermediate angles such as $\pi/4<\theta\leqslant 3\pi/4$ and $3\pi/4\leqslant\theta\leqslant\pi$, $0\leqslant\theta\leqslant\pi/4$, $\langle S\rangle$ is directly proportional to the tangent function: $\tan(\pi/2-\theta)$ and $\tan\theta$, respectively. Taking this into consideration,one can determine the equation for $\langle S\rangle$

$$\langle S\rangle=\begin{cases}\dfrac{\tan\theta}{2}, & 0<\theta\leqslant\pi/4\\[2mm] 1-\dfrac{\tan(\pi/2-\theta)}{2}, & \pi/4<\theta\leqslant\pi<2\\[2mm] 1-\dfrac{\tan(\pi/2-\theta)}{2}, & \pi/2<\theta\leqslant 3\pi/4\\[2mm] 2+\dfrac{\tan\theta}{2}, & 3\pi/4<\theta\leqslant\pi.\end{cases} \tag{B1}$$

For a zero angle θ the source region vanishes $\langle S\rangle=0$ since no charge flows around the obstacle corner (the obstacle is an infinite straight line), consequently $A_S=0$, $F_1=0$. For this case an excitation wave attaches to the obstacle (straight line) even at $\lambda=0$. Thus the functions $P_L/L_{\rm crit}$ and $A_L/L_{\rm crit}^2$ are of the order of $O(1)$ at $\theta=0$ and without loss of generality one can assume that F_2 and F_3 are equal to $L_{\rm crit}$ and $L_{\rm crit}^2$, respectively.

Figure 5 illustrates the details of the geometric considerations when the obstacle is aligned parallel to the wave-front velocity vector ($\theta=\pi$). Shown is the time dependent development of the source region (shaded squares of length L_f at $t=0$ and $t=t_1$, $A_S=2L_f^2$) of the incident wave front adjacent to the obstacle surface and the load boundary-layer regions three boundary-layer regions shown in Fig. 5(B), growing to five boundary-layer regions shown in Fig. 5(C)] We assume the boundary-layer formation time to be $T=2\Delta t$ [Fig. 5(D)] and approximate the development of the boundary-layer area as shown in Fig. 5(D) so that $A_L=L_{\rm crit}^2(3\Delta t/4+15\Delta t/2)/2\Delta t=33/8L_{\rm crit}^2$.

Leakage of charge occurs from the perimeter of the boundary-layer area [KMNQ in Figs. 5(B), 5(C)]. We approximate the development of the perimeter as shown in Fig. 5(D) and the time averaged value of $P_L=L_{\rm crit}(5\Delta t/4+21\Delta t/2)/2\Delta t=47/8L_{\rm crit}$.

Figure 6 illustrates the geometric details for $\theta=\pi/2$ when $A_S=L_f^2$, $A_L=L_{\rm crit}^2(\Delta t/2+9\Delta t/4)/\Delta t=11/4L_{\rm crit}^2$ and $P_L=L_{\rm crit}(3\Delta t/4+12\Delta t/4)/\Delta t=15/4L_{\rm crit}$. Equating $\Phi_i(\theta)$ with the coefficients A_S, A_L and P_L in balance Eq. (7) for $\theta=0$, $\theta=\pi/2$ and $\theta=\pi$, we have

$$A_S=L_f^2(7\langle S\rangle^2-\langle S\rangle^4)/6$$

$$P_L=L_{\rm crit}[1+(313\langle S\rangle^2-49\langle S\rangle^4)/96],$$

$$A_L=L_{\rm crit}^2[1+(199\langle S\rangle^2-31\langle S\rangle^4)/96]. \tag{B2}$$

[1] A. T. Winfree, *When Time Breaks Down: The Three-Dimensional Dynamics of Electrochemical Waves and Cardiac Arrhythmias* (Princeton University Press, Princeton, 1987).
[2] *Chemical Waves and Patterns*, edited by R. Kapral and K. Showalter (Kluwer, Dordrecht, Netherlands, 1995).
[3] A. M. Pertsov, J. M. Davidenko, R. Salomoncz, W. T. Baaxter, and J. Jalife, Cir. Res. **72**, 631 (1993).
[4] I. S. Balakhovsky, Biofizika **10**, 1063 (1965).
[5] V. I. Krinsky, Biofizika **11**, 676 (1966).
[6] A. M. Pertsov, A. V. Panfilov, and F. U. Medvedeva, Biofizika **28**, 100 (1983).
[7] A. M. Pertsov, E. A. Ermakova, and E. E. Shnol, Physica D **44**, 178 (1990).
[8] A. V. Panfilov and J. P. Keener, J. Theor. Biol. **163**, 439 (1993).
[9] K. Agladze, J. P. Keener, S. C. Muller, and A. V. Panfilov, Science **264**, 1746 (1994).
[10] M. Gomez-Gesteria, J. L. del Castillo, M. E. Varquez-Iglesias, V. Perez-Munuzuri, and V. Perez-Villar, Phys. Rev. E **50**, 4646 (1994).
[11] A. S. Mikhailov, *Foundations of Synergetics 1. Distributed Active Systems* (Springer, Berlin, 1990).
[12] J. M. Starobin, Yu. I. Zilberter, and C. F. Starmer, Physica D **70**, 321 (1994).
[13] L. A. Ostriovskii and V. G. Yakhno, Biofizika **20**, 498 (1975).
[14] R. D. Richtmayer, *Difference Methods for Initial-value Problems* (Interscience, New York, 1957).